Kinetic Growth of Self-Formed In_2O_3 Nanodots *via* Phase Segregation: Ni/InAs System

Chin-Hung Liu,[†] Szu-Ying Chen,[†] Cheng-Ying Chen,[‡] Jr-Hau He,[‡] Lih-Juann Chen,[†] Johnny C Ho,[§,*] and Yu-Lun Chueh[†,*]

[†]Department of Materials Science & Engineering, National Tsing Hua University, No. 101, Sec. 2 Kuang-Fu Road, Hsinchu 30013, Taiwan, [‡]Institute of Photonics and Optoelectronics, National Taiwan University, Taipei 10617, Taiwan, and [§]Department of Physics and Materials Science, City University of Hong Kong, Tat Chee Avenue, Kowloon, Hong Kong SAR, China

ABSTRACT Highly compact In_2O_3 nanodots with uniform size were synthesized by a novel approach *via* direct annealing of Ni/InAs samples at temperatures over 250 °C. The In_2O_3 nanodots were formed by solid diffusion between nickel and indium arsenide (InAs) and phase segregation *via* a catalyst-assisted kinetic process. By controlling the annealing time and ambient conditions, the size and density of In_2O_3 nanodots can be controlled. From photoluminescence (PL) measurements, two distinct peaks located at ~430 and ~850 nm, corresponding to 2.9 and 1.5 eV for In_2O_3 nanodots, can be observed. The peaks originate from radioactive recombination centers such as oxygen vacancies or indium interstitials inside In_2O_3 nanodots. The periodic array of Ni microdiscs with diameters and interdisc spacing of ~5 and ~10 μm on InAs substrate surface prepared by a photolithography process demonstrated the precise control of In_2O_3 nanodots at a specific position. Applications for precisely locating optoelectronic nanodevices in combination with electronic nanodevices are envisioned.

KEYWORDS: In_2O_3 nanodot · catalyst-assisted kinetic process · Ni_xInAs · InAs · phase segregation

Nanostructures are defined as materials with at least one geometric dimension less than 100 nm. Many fascinating phenomena and unexpected properties, which differ from their bulk counterparts, have been explored as their dimensions shrink down to nano- or sub-nanometer regions. In recent years, a multitude of approaches have been applied to synthesize various nanostructures, including nanobelts,[1,2] nanowires,[3] and nanodots[4,5] with tunable optical and electrical properties due to "quantum effects", such as size-dependent excitation,[6,7] quantized conductance,[8] single-electron tunneling,[9] and metal–insulator transition.[10] Nanomaterials with these extraordinary properties can be incorporated into optoelectrical devices and system-on-chip (SOC) modules.[11]

Indium oxide (In_2O_3) is an important transparent material with a wide band gap (E_g) of ~3.6 eV and has been used for numerous applications in optical and electrical devices, including solar cells,[12,13] gas sensors,[14–16] and light-emitting diode devices.[17,18] Several methods have been proposed for the growth of In_2O_3 nanodots, such as templates-assisted growth,[13] sol–gel synthesis,[14] and laser ablation.[19] These methods, however, suffer from several problems, such as low yielding rate, impurity contaminations, non-uniform size distribution, and material damage. In this paper, we present a novel approach to synthesize highly compact In_2O_3 nanodots from an InAs wafer by direct annealing of the Ni/InAs sample at temperatures over 250 °C. From experimental results, the formation mechanism of these In_2O_3 nanodots is believed to result from a catalyst-assisted growth, which is based on the phase segregation of In and As atoms out of a saturated Ni_xInAs underlying layer to form In_2O_3 nanodots with residual oxygen molecules during annealing, while the As atoms are found to not be involved in the formation of In_2O_3 nanodots. The size and density of In_2O_3 nanodots are controllable, depending on different annealing time and ambient conditions. This research also demonstrates the possibility of patterned segregation sites for In_2O_3 nanodots.

RESULTS AND DISCUSSION

The process of catalyst-assisted growth of highly compact In_2O_3 nanodots with uniform size is schematically illustrated in Figure 1a. A 50 nm thick Ni layer was deposited onto native oxide-free crystalline InAs(100) substrates by electron-beam evaporation with a deposition rate of ~0.03 nm/s. The samples were then heated by rapid thermal annealing (RTA) at temperatures from 250 to 350 °C in different annealing ambient condition. Highly compact In_2O_3 nanodots

* Address correspondence to ylchueh@mx.nthu.edu.tw, johnnyho@cityu.edu.hk.

Received for review June 8, 2011 and accepted July 24, 2011.

Published online July 25, 2011
10.1021/nn202109u

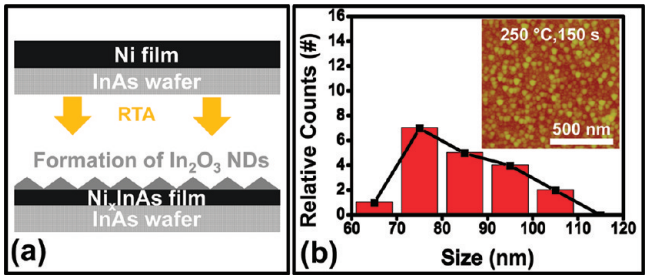

Figure 1. (a) Schematic for the formation of In_2O_3 nanodots *via* a catalyst-assisted process. (b) Size distribution of In_2O_3 nanodots after annealing at 250 °C for 150 s. Inset shows the corresponding AFM image of In_2O_3 nanodots.

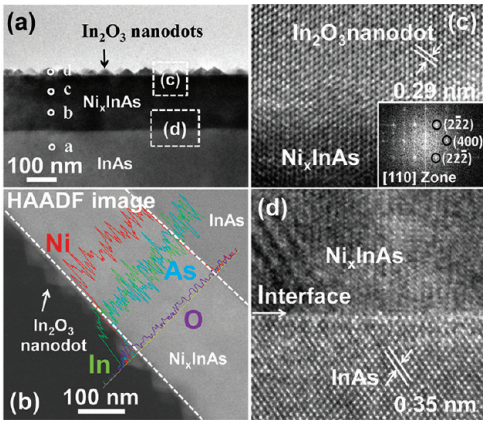

Figure 2. (a) Low-magnification cross-section TEM image of Ni/InAs after annealing at 250 °C for 150 s. (b) Corresponding HAADF image and compositional profiles of nickel, indium, arsenide, and oxygen. (c) High-resolution TEM image of a single In_2O_3 nanodot taken from region (c) in Figure 2a. Inset shows the fast Fourier transform diffraction pattern of the In_2O_3 nanodot with a zone axis of [110]. (d) High-resolution TEM image of the Ni_xInAs/InAs interface taken from region (d) in Figure 2a, revealing the sharp interface.

were then formed upon the surface of Ni_xInAs/InAs substrates. It is worthwhile to mention that a Ni_xInAs film layer will be formed prior to the formation of In_2O_3 nanodots. The surface morphology and distribution of In_2O_3 nanodots were characterized by atomic force microscopy (AFM). Figure 1b shows the statistical size distribution of In_2O_3 nanodots ranging from 60 to 110 nm with an average size of 80 nm for a Ni (50 nm)/InAs sample annealed at 250 °C for 150 s. The corresponding AFM image shown in the inset of Figure 1b reveals that the density of dots is $\sim 4 \times 10^9$ dots/cm^2. The structural analysis of In_2O_3 nanodots was carried out with a transmission electron microscope (TEM). Figure 2a shows a low-magnification cross-section TEM image of an In_2O_3 nanodot/Ni_xInAs/InAs sample. The quantitative compositional analysis based on energy-dispersive spectroscopy (EDS) at different positions marked as positions a, b, c, and d in Figure 2a and the corresponding results are summarized in Table 1. The compositions of nanodots are ~41 and ~59 at % (atomic concentration) for indium and oxygen, respectively, which agree with

TABLE 1. Quantitative EDS Data from Selective Regions in Figure 2a

position	In (atomic %)	As (atomic %)	Ni (atomic %)	O (atomic %)
a	43	57	<0.1	<0.1
b	25	26	49	<0.1
c	21	27	52	<0.1
d	41	<0.1	<0.1	59
e	<0.1	<0.1	100	<0.1
f	3	7	71	11
g	45	55	<0.1	<0.1
h	<0.1	<0.1	100	<0.1
i	22	27	51	<0.1

the ratio of In_2O_3 being 2:3. In addition, atomic concentrations at two other positions, b and c, inside the Ni_xInAs metallic alloy layer show average concentrations of ~49, ~25, and ~26% for Ni, In, and As, corresponding to the atomic ratio of Ni/In/As being 2:1:1. The elemental profiles shown in Figure 2b clearly confirm that the compositional distributions of dots only contain indium and oxygen. Figure 2c shows a high-resolution transmission electron microscope (HRTEM) image taken from the rectangular region c in Figure 2a, indicating the single-crystalline nature of all nanodots, which are epitaxially grown on the Ni_xInAs layer. The lattice spacing of 0.29 nm, corresponding to (111) plane of cubic In_2O_3 (phase group of *Ia*3 with lattice constant of $a = 0.117$ nm), can be identified. Inset in Figure 2c shows the corresponding selected area diffraction pattern with the zone axis of [110] extracted by fast Fourier transform (FFT). Note that abruptly a sharp interface between Ni_xInAs and InAs occurs, suggesting that the reaction of Ni/InAs alloy is limited by how fast the Ni atoms can diffuse into InAs, namely, diffusion control. The similar behavior can be found in many metal/Si systems, especially the Ni/Si system.[20,21]

To understand the detailed formation mechanism of In_2O_3 nanodots, the Ni/InAs alloy was annealed at different temperatures from 200 to 350 °C for 150 s in a vacuum of $\sim 10^{-2}$ Torr, as shown in Figure 3a–c. No nanodot can be observed if the annealing temperature is below 200 °C, while the diffusion of Ni into InAs still remains, thereby forming the Ni_xInAs alloy

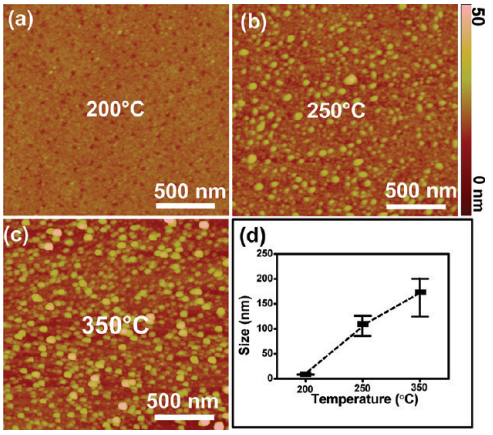

Figure 3. AFM images of Ni/InAs sample after annealing at (a) 200 °C, (b) 250 °C, and (c) 350 °C for 150 s. (d) Statistical size distributions of In_2O_3 nanodots synthesized at different annealing temperatures.

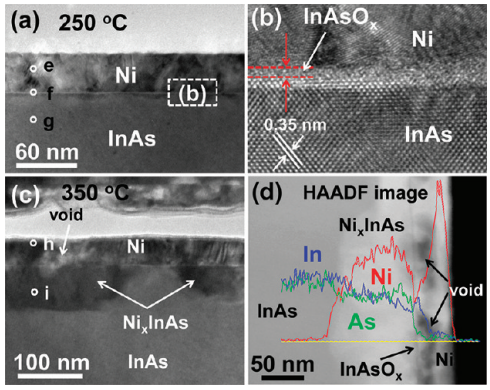

Figure 4. Effect of $InAsO_x$ oxide layer on the formation of In_2O_3 nanodots. (a) Low-magnification cross-section TEM image of Ni/$InAsO_x$/InAs after annealing at 250 °C for 100 s. (b) High-resolution TEM image of selected region taken from (a). (c) Low-magnification cross-section TEM image of Ni/$InAsO_x$/InAs after annealing at 350 °C for 100 s. (d) Corresponding HAADF image and elemental profiles of nickel, indium, arsenide, and oxygen across Ni/$InAsO_x$/InAs, in which the voids can be clearly distinguished.

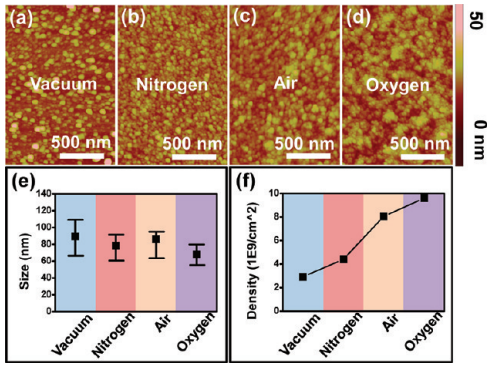

Figure 5. Ambient effects on the distribution of size and density. AFM images of Ni/InAs samples annealed at 250 °C for 100 s in (a) vacuum, (b) nitrogen, (c) atmosphere, and (d) ambient oxygen. (e,f) Size and density distributions in different ambient conditions.

layer with abrupt interface (Supporting Information, Figure S1). As depicted in Figure 3b,c, uniform and dense In_2O_3 nanodots were grown at annealing temperatures over 250 °C. At the annealing temperature of 350 °C, the size and density of nanodots increase accordingly. The corresponding statistical evolution of nanodot size in Figure 3d reveals that the size of nanodots increases from ~100 to ~150 nm with annealing temperature increased from 250 to 350 °C. The results indicate that the formation mechanism of In_2O_3 nanodots follows catalyst-assisted growth, which is based on the phase segregation of In and As atoms out of the underlying Ni_xInAs layer once Ni_xInAs reaches the saturated state. This phase segregation behavior of In and As atoms out of the Ni_xInAs layer is similar to segregation of Si out of the disilicide system at elevated annealing temperature.[22] Similar segregation of In has been found in the Ni/InP system.[23] Once the In and As atoms are segregated from Ni_xInAs layer, In atoms tend to form In_2O_3 nanodots with residual oxygen molecules during the annealing while As atoms prefer to become vapor rather than be involved in the oxidation reaction. The heat of evaporation energy (5.1 kJ/mol)[24] for As is much lower compared to that of In (236.6 kJ/mol)[25] and much higher free energy ($-259.3 + 0.1T - 2.6 \times 10^{-3}\ T \ln T$),[26] with O compared to that with In ($-909.4 + 0.3T$ kJ/mol).[27] Therefore, the system prefers to form In_2O_3 during the oxidation reaction. This result is also consistent with EDS findings for In_2O_3 nanodots, as illustrated in Table 1, where the concentration of As atoms is almost zero at position d in Figure 2a. To confirm our proposed mechanism, a Ni layer with the same thickness was deposited on the same InAs substrate with an $InAsO_x$ layer as the barrier layer intentionally formed between Ni and InAs *via* the direct oxidation of InAs wafer, as shown in Figure 4a, in which a distinctly different contrast between Ni and InAs can be observed. Figure 4b shows a high-resolution TEM image of the $InAsO_x$ layer with a thickness of ~2 nm taken from the rectangular area of Figure 4a, revealing the amorphous feature of $InAsO_x$. The EDS quantitative analysis of data obtained at layers marked e, f, and g is shown in Table 1. Figure 4c shows a TEM image for the sample after annealing at 350 °C for 100 s. Figure 4d shows the corresponding HAADF image with elemental profiles of each layer and quantitative analysis at positions h and i, as shown in Table 1. Note that only Ni atoms can partially diffuse into InAs to form Ni_xInAs during annealing, leading to the formation of voids. It indicates that the $InAsO_x$ layer can indeed retard the diffusion of Ni atoms into InAs. No formation of In_2O_3 nanodots was observed at this annealing condition, revealing that the segregation of In and As atoms out of the Ni_xInAs layer does not occur in this case, which further confirms that the compositional saturation of the Ni_xInAs is not reached yet because of the existence of the $InAsO_x$ barrier layer. In addition, we find that In_2O_3

nanodots can only be formed on the InAs system using Ni as a capping layer, while no In_2O_3 nanodots can be formed using Au or Pt as capping layers.

To shed light on the ambient effect on the formation of the In_2O_3 nanodots, the Ni(50 nm)/InAs samples were annealed at 250 °C for 150 s in different annealing ambient conditions from vacuum with a base pressure of 1×10^{-3} Torr, to nitrogen, atmosphere, and pure oxygen environments. The corresponding AFM results with the same scale bar are shown in Figure 5a–d for comparison. Figure 5e,f shows the results of size distribution and density evolution derived from AFM results. The size of In_2O_3 nanodots decreases from ~85 to ~65 nm with an increase of oxygen content in the annealing ambient condition, while the density of In_2O_3 is monotonically increased from $\sim 3 \times 10^9$ to $\sim 9 \times 10^9$ dots/cm^2. At the same annealing temperature and time, the amount of segregated In atoms out of Ni_xInAs should be the same while the nucleation size of In_2O_3 nanodots may highly depend on the amount of oxygen content. The higher the concentration of oxygen during formation of the In_2O_3 nanodot, the smaller the critical size for nucleation of In_2O_3 nanodots. It is the reason why the density increases with decreasing size at the same annealing condition with higher oxygen concentration (Supporting Information, Table S1). Therefore, we believe the In_2O_3 nanodots with a few nanometer ranges should be possibly achieved upon precise control of annealing conditions, such as annealing time or ambient conditions. In addition, the difference in thickness of the Ni layer will also influence the solid diffusion of Ni into InAs and phase segregation, thereby affecting the formation of In_2O_3 nanodots. If the thickness of the Ni layer is increased from 50 to 100 nm, the annealing time for the formation of In_2O_3 nanodots is also increased at the same annealing temperature (Supporting Information, Figure S2).

Photoluminescence (PL) spectra were measured at room temperature with the excitation wavelength of 325 nm, as shown in Figure 6 for In_2O_3 nanodot/Ni_xInAs/InAs and pure InAs samples. Two distinct peaks located at ~430 and ~850 nm, corresponding to 2.9 and 1.5 eV, respectively, for In_2O_3 nanodot/Ni_xInAs/InAs samples can be observed. The energies for two emission peaks are much larger than the band gap transition of InAs, for which InAs has a direct band gap of ~0.35 eV. Therefore, emitting peaks from the underlying InAs substrate can be ruled out, while the emission from band to band excitation of In_2O_3 is forbidden due to the indirect band gap nature with a band gap of ~3.6 eV, corresponding to a wavelength of ~345 nm. In addition, emission from the Ni_xInAs layer is also unlikely due to the metallic property. Accordingly, we can conclude that these two emitting peaks originate from radioactive recombination centers such as oxygen vacancies or indium interstitials inside In_2O_3 nanodots.[28] Moreover, the smaller In_2O_3 particles prefer the existence of more oxygen vacancies because of larger surface-to-volume ratio and thereby higher

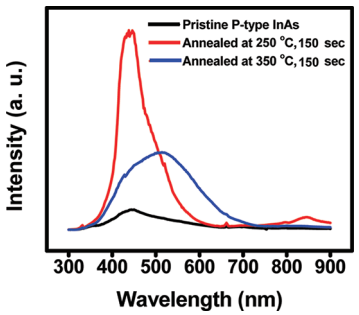

Figure 6. Photoluminescence spectra of Ni/InAs samples after annealing at 250 and 350 °C for 150 s and pure InAs sample for comparison. Red, blue, and black lines represent PL spectra for the Ni/InAs samples after annealing at 250 and 350 °C for 150 s and without annealing, respectively.

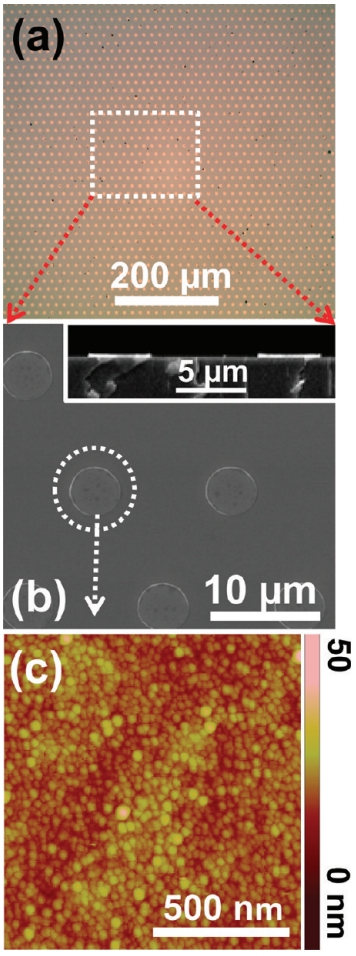

Figure 7. Demonstration of precisely controlling the growth site of In_2O_3 nanodots on InAs substrate. (a) Optical image of large-scale (>0.5 mm^2) ordered Ni microdisc pattern achieved by photolithography technique. (b) Corresponding SEM image with the size and interdisc spacing being ~5 and ~10 μm for each microdisc, respectively. The cross-section view of these Ni microdiscs is shown in the inset. (c) AFM image of each Ni microdisc after annealing at 350 °C for 150 s.

intensity of PL emission. A very weak and broad peak located at 430 nm, corresponding to 2.9 eV for the pure InAs wafer, which originated from a native In_2O_3 oxide, further confirms the interpretation. PL property is further studied by annealing In_2O_3 nanodots with different annealing times. As the size of In_2O_3 nanodots increases with annealing time, the PL intensity becomes weaker with a little shift of peak position. The decease of PL intensity for In_2O_3 nanodots with larger particle size at elongated annealing time can be observed as the reduction of surface ratio and concentration of oxygen vacancies. A similar result is also observed in ZnO nanoparticles.[29]

A unique advantage of our processes is to precisely control positions of In_2O_3 nanodots. To demonstrate this concept, a periodic Ni microdisc array with the diameter and interdisc distance of ~5 and ~10 μm, respectively, were patterned on the InAs substrate surface by conventional photolithography and lift-off processes. The corresponding optical microscope (OM) and SEM images are shown in Figure 7a,b, respectively. Inset in Figure 7b shows the cross-section view of these periodic Ni microdisc arrays. After annealing at 350 °C for 150 s, the In_2O_3 nanodots can be found only on patterned region, as can be seen from the AFM image in Figure 7c. This patterning technique can be applied for making systems on an InAs chip to enhance performance of related optoelectrical devices.

CONCLUSIONS

In summary, we present a novel approach to synthesize highly uniform In_2O_3 nanodots by directly annealing a Ni/InAs sample at temperatures over 250 °C. The formation mechanism of In_2O_3 nanodots is understood in terms of phase segregation and solid diffusions between nickel and InAs *via* a catalyst-assisted process. The sizes of In_2O_3 nanodots decrease from ~85 to ~65 nm with the increase of oxygen-containing ambient condition, while the density of In_2O_3 is monotonically increased from $\sim 3 \times 10^9$ to $\sim 9 \times 10^9$ dots/cm^2. Additionally, PL spectra were obtained at room temperature for In_2O_3 nanodots. Two distinct peaks located at ~430 and ~850 nm, corresponding to 2.9 and 1.5 eV, respectively, can be observed, which are originated from some radioactive recombination centers such as oxygen vacancies or indium interstitials inside In_2O_3 nanodots. The decease of PL intensity for In_2O_3 nanodots with larger particle size at elongated annealing time can be observed due to the reduction of surface ratio and concentration of oxygen vacancies. The advantage on how to precisely control positions of In_2O_3 nanodots with a pattern of periodic Ni microdiscs based on our synthesis approach was demonstrated, which has potential applications in precisely locating optoelectronic nanodevices in combination with electronic nanodevices.

METHODS

InAs wafers were cleaned by acetone and isopropyl alcohol. Subsequently, wafers were dipped into dilute HF solution (HF/H_2O = 1:10 v/v) for 20 s to totally remove the native oxide layer. The Ni layer was deposited by an E-gun evaporation system with deposition rate of ~0.03 nm/s. The samples were then heated by rapid thermal annealing (RTA) at temperatures from 250 to 350 °C in different annealing ambient conditions. The surface morphologies were examined by atomic force microscopy (AFM, Digital Instrument 3100). Field-emission transmission electron microscope (JEM-3000F, operated at 300 kV with point-to-point resolution of 0.17 nm) equipped with an energy-dispersion spectrometer (EDS) was used to obtain the information of the microstructures and the chemical compositions. Room temperature PL measurements were performed with excited laser wavelength of 290 nm. Optical microscopy (OM) was also applied to examine the surface conditions of the samples. Periodic Ni microdisc arrays with the diameter and interdisc distance of ~5 and ~10 μm were patterned on the InAs substrate surface by conventional photolithography and lift-off processes.

Acknowledgment. This research was supported by the National Science Council through Grant No. NSC 100-2628-E-007-003-, NSC 98-2112-M-007-025-MY3, and by the General Research Fund of the Research Grants Council of Hong Kong SAR, China, under Project No. CityU 101210.

Supporting Information Available: The TEM results at annealing temperature of 200 °C and AFM results of Ni/InAs sample with Ni thickness of 100 nm annealed at 350 °C with different annealing time. This material is available free of charge *via* the Internet at http://pubs.acs.org.

REFERENCES AND NOTES

1. Pan, Z. W.; Dai, Z. R.; Wang, Z. L. Nanobelts of Semiconducting Oxides. *Science* **2001**, *291*, 1947–1949.
2. Jeong, J. S.; Lee, J. Y.; Lee, C. J.; An, S. J.; Yi, G. C. Synthesis and Characterization of High-Quality In_2O_3 Nanobelts *via* Catalyst-Free Growth Using a Simple Physical Vapor Deposition at Low Temperature. *Chem. Phys. Lett.* **2004**, *384*, 246–250.
3. Peng, X. S.; Wang, Y. W.; Zhang, J.; Wang, X. F.; Zhao, L. X.; Meng, G. W.; Zhang, L. D. Large-Scale Synthesis of In_2O_3 Nanowires. *Appl. Phys. A: Mater. Sci. Process.* **2002**, *74*, 437–439.
4. Lei, Y; C., W. K.; Weissmuller, J; Wilde, G; Sun, H P; Pan, X. Q. Ordered Arrays of Highly Oriented Single-Crystal Semiconductor Nanoparticles on Silicon Substrates. *Nanotechnology* **2005**, *16*, 1892.
5. Narayanaswamy, A.; Xu, H.; Pradhan, N.; Kim, M.; Peng, X. Formation of Nearly Monodisperse In_2O_3 Nanodots and Oriented-Attached Nanoflowers: Hydrolysis and Alcoholysis *vs* Pyrolysis. *J. Am. Chem. Soc.* **2006**, *128*, 10310–10319.
6. Alivisatos, A. P. Semiconductor Clusters, Nanocrystals, and Quantum Dots. *Science* **1996**, *271*, 933–937.
7. Murray, C. B.; Kagan, C. R.; Bawendi, M. G. Synthesis and Characterization of Monodisperse Nanocrystals and Close-Packed Nanocrystal Assemblies. *Annu. Rev. Mater. Sci.* **2000**, *30*, 545–610.
8. Krans, J. M.; van Ruitenbeek, J. M.; Fisun, V. V.; Yanson, I. K.; de Jongh, L. J. The Signature of Conductance Quantization in Metallic Point Contacts. *Nature* **1995**, *375*, 767–769.
9. Likharev, K. K.; Claeson, T. Single Electronics. *Sci. Am.* **1992**, *266*, 80–85.

10. Markovich, G.; Collier, C. P.; Henrichs, S. E.; Remacle, F.; Levine, R. D.; Heath, J. R. Architectonic Quantum Dot Solids. *Acc. Chem. Res.* **1999**, *32*, 415–423.
11. Singh-Gasson, S.; Green, R. D.; Yue, Y.; Nelson, C.; Blattner, F.; Sussman, M. R.; Cerrina, F. Maskless Fabrication of Light-Directed Oligonucleotide Microarrays Using a Digital Micromirror Array. *Nat. Biotechnol.* **1999**, *17*, 974–978.
12. Hara, K.; Horiguchi, T.; Kinoshita, T.; Sayama, K.; Sugihara, H.; Arakawa, H. Highly Efficient Photon-to-Electron Conversion with Mercurochrome-Sensitized Nanoporous Oxide Semiconductor Solar Cells. *Sol. Energy Mater. Sol. Cells* **2000**, *64*, 115–134.
13. Katoh, R.; Furube, A.; Yoshihara, T.; Hara, K.; Fujihashi, G.; Takano, S.; Murata, S.; Arakawa, H.; Tachiya, M. Efficiencies of Electron Injection from Excited N3 Dye into Nanocrystalline Semiconductor (ZrO_2, TiO_2, ZnO, Nb_2O_5, SnO_2, In_2O_3) Films. *J. Phys. Chem. B* **2004**, *108*, 4818–4822.
14. Fan, Z.; Lu, J. G. Gate-Refreshable Nanowire Chemical Sensors. *Appl. Phys. Lett.* **2005**, *86*, 123510-3.
15. Gurlo, A.; Ivanovskaya, M.; Bârsan, N.; Schweizer-Berberich, M.; Weimar, U.; Göpel, W.; Diéguez, A. Grain Size Control in Nanocrystalline In_2O_3 Semiconductor Gas Sensors. *Sens. Actuators, B* **1997**, *44*, 327–333.
16. Du, N.; Zhang, H.; Chen, B. D.; Ma, X. Y.; Liu, Z. H.; Wu, J. B.; Yang, D. R. Porous Indium Oxide Nanotubes: Layer-by-Layer Assembly on Carbon-Nanotube Templates and Application for Room-Temperature NH_3 Gas Sensors. *Adv. Mater.* **2007**, *19*, 1641–1645.
17. Kim, H.; Horwitz, J. S.; Kushto, G. P.; Qadri, S. B.; Kafafi, Z. H.; Chrisey, D. B. Transparent Conducting Zr-Doped In_2O_3 Thin Films for Organic Light-Emitting Diodes. *Appl. Phys. Lett.* **2001**, *78*, 1050–1052.
18. Ju, S.; Facchetti, A.; Xuan, Y.; Liu, J.; Ishikawa, F.; Ye, P.; Zhou, C.; Marks, T. J.; Janes, D. B. Fabrication of Fully Transparent Nanowire Transistors for Transparent and Flexible Electronics. *Nat. Nanotechnol.* **2007**, *2*, 378–384.
19. Murali, A.; Barve, A.; Leppert, V. J.; Risbud, S. H.; Kennedy, I. M.; Lee, H. W. H. Synthesis and Characterization of Indium Oxide Nanoparticles. *Nano Lett.* **2001**, *1*, 287–289.
20. Chueh, Y. L.; Chou, L. J.; Cheng, S. L.; Chen, L. J.; Tsai, C. J.; Hsu, C. M.; Kung, S. C. Synthesis and Characterization of Metallic $TaSi_2$ Nanowires. *Appl. Phys. Lett.* **2005**, *87*, 223113-3.
21. Chueh, Y. L.; Ko, M. T.; Chou, L. J.; Chen, L. J.; Wu, C. S.; Chen, C. D. $TaSi_2$ Nanowires: A Potential Field Emitter and Interconnect. *Nano Lett.* **2006**, *6*, 1637–1644.
22. Chueh, Y. L.; Ford, A. C.; Ho, J. C.; Jacobson, Z. A.; Fan, Z.; Chen, C. Y.; Chou, L. J.; Javey, A. Formation and Characterization of Ni_xInAs/InAs Nanowire Heterostructures by Solid Source Reaction. *Nano Lett.* **2008**, *8*, 4528–4533.
23. Mohney, S. E.; Chang, Y. A. Interfacial Reactions and Phase-Stability in the Ni/InP System. In *Advanced Metallization for Devices and Circuits - Science, Technology and Manufacturability*; Murarka, S. P., Katz, A., Tu, K. N., Maex, K., Eds.; Materials Research Society: Pittsburgh, PA, 1994; Vol. 337, pp 393−398.
24. Gokcen, N. The As (Arsenic) System. *J. Phase Equilib.* **1989**, *10*, 11–22.
25. Macur, G. J.; Edwards, R. K.; Wahlbeck, P. G. Multiple Knudsen Cell Effusion. Enthalpies of Vaporization of Indium and Gallium1. *J. Phys. Chem.* **1966**, *70*, 2956–2965.
26. Chen, C.; Zhang, L.; Jahanshahi, S. Thermodynamic Modeling of Arsenic in Copper Smelting Processes. *Metall. Mater. Trans. B* **2010**, *41*, 1175–1185.
27. Panek, Z.; Fitzner, K. Gibbs Free Energy of Formation of In_2O_3 and $CaIn_2O_4$. *Thermochim. Acta* **1986**, *97*, 171–176.
28. Poznyak, S. K.; Golubev, A. N.; Kulak, A. I. Correlation between Surface Properties and Photocatalytic and Photoelectrochemical Activity of In_2O_3 Nanocrystalline Films and Powders. *Surf. Sci.* **2000**, *454−456*, 396–401.
29. Du, Y.; Zhang, M.-S.; Hong, J.; Sheen, Y.; Chen, Q.; Yin, Z. Structural and Optical Properties of Nanophase Zinc Oxide. *Appl. Phys. A: Mater. Sci. Process.* **2003**, *76*, 171–176.